

Characterizing the weak topological properties: Berry phase point of view

Yukinori Yoshimura¹, Ken-Ichiro Imura¹, Takahiro Fukui², and Yasuhiro Hatsugai³

¹*Department of Quantum Matter, AdSM, Hiroshima University, Higashi-Hiroshima 739-8530, Japan*

²*Department of Physics, Ibaraki University, Mito 310-8512, Japan and*

³*Institute of Physics, University of Tsukuba, 1-1-1 Tennodai, Tsukuba, Ibaraki 305-8571, Japan*

(Dated: May 20, 2014)

We propose classification schemes for characterizing two-dimensional topological phases with non-trivial weak indices. Here, “weak” implies that the Chern number in the corresponding phase is trivial, while the system shows edge states along specific boundaries. As concrete examples, we analyze different versions of the so-called Wilson-Dirac model with (i) anisotropic Wilson terms, (ii) next nearest neighbor hopping terms, and (iii) a superlattice generalization of the model, here in the tight-binding implementation. For types (i) and (ii) a graphic classification of *strong* properties is successfully generalized for classifying *weak* properties. As for type (iii), weak properties are attributed to quantized Berry phase π along a Wilson loop.

PACS numbers: 73.20.-r, 73.22.-f, 61.72.Lk

I. INTRODUCTION

The emerging field of the topological insulator has fascinated a broad perspective of physicists, both theoretical¹ and experimental,² because its main idea was simple³ and the resulting topological properties are robust against disorder; *i.e.*, in a sense, *universal*. It has proven to be realistic and “almost ubiquitous”.⁴ It even exists naturally.⁵ In addition to be simple, robust and realistic, it may also be useful. The “dark” surface of the so-called “weak” topological insulators (WTI) could be etched and patterned, in order to realize a topologically protected nanocircuit.⁶

In contrast to the more standard “strong” topological insulator (STI) that exhibits a single protected Dirac cone (a topologically protected metallic state) on its surface, the WTI is called weak, because it exhibits an even number of Dirac cones that are not necessarily protected. A sufficient amount and a type of disorder may wash out characteristic features of the surface Dirac states.^{7,8} However, this does not mean that disorder has destroyed all the topological nature of the WTI phase. Under the fragile, and damaged surface states, topological non-triviality is simply *hidden*; it continues to survive, and manifests when a proper circumstance arrives, *e.g.*, when an appropriate nano-pattern is either formed artificially or naturally⁹ on the cleaved surface, or in the bulk (in the form of a dislocation line), paving the way for opening a 1D protected “perfectly conducting” channel.¹⁰

Unfortunately, there have not been many experimental papers that have reported on the nature of such WTI, based on a study of stoichiometric compounds.¹¹ In this regard, it would be worth mentioning the so-called topological crystalline insulator (TCI).^{12,13} Unlike for the more standard \mathbb{Z}_2 topological insulator, the spin-orbit coupling is not indispensable for TCI. TCI is protected by crystalline symmetry,¹⁴ and exhibits an even number of Dirac cones on its surface; *therefore, regarded as a variant of WTI*. Such surface states of the TCI have been observed experimentally.^{15,16}

Another context in which the WTI has started to be much discussed is the superlattice of a STI and an ordinary insulator (OI). Such a superlattice has been originally proposed for realizing a 3D Weyl semimetal by adjusting the ratio of the two constituent layers.¹⁷ More recently, there are increasing number of such a superlattice generalization of the topological insulator, and a possibility of realizing and even *controlling* (by changing the superlattice structure) various WTI phases^{18–20} that has seemed to be hard to be realized in stoichiometric materials.

Here in this paper, we focus on 2D models, for simplicity, and attempt to make detailed analysis and comparison of the WTI phases realized in superlattice and non-superlattice models. We study variants of the so-called Wilson-Dirac model showing weak as well as strong topological phases. Here, “strong” means that the ground state is characterized by a nontrivial Chern number, while in the “weak” case the same is characterized by a vanishing Chern number, yet shows edge states along specific boundaries. We consider such variations of the Wilson-Dirac model as with (i) anisotropic Wilson terms, (ii) next nearest neighbor hopping terms, and also (iii) a superlattice generalization of the model. We show that protection of the edge states in such WTI phases stems from quantization of the Berry phase on an appropriate Wilson loop. This mechanism of topological protection is much related to that of graphene’s (flat band) edge modes in the so-called “zigzag” edge geometry.^{21,22}

The paper is organized as follows. In Sec. II we introduce our models and summarize their basic properties. A graphic way to classify weak and strong topological phases is outlined in Sec. III. Discussion on the superlattice model is started in Sec. IV. In Sec. V we study the structure of its phase diagram in detail, and show some analytic formulas for phase boundaries. Weak topological phases in the superlattice model are further analyzed from the viewpoint of quantized Berry phase associated with a Wilson loop. Sec. VI is devoted to conclusions.

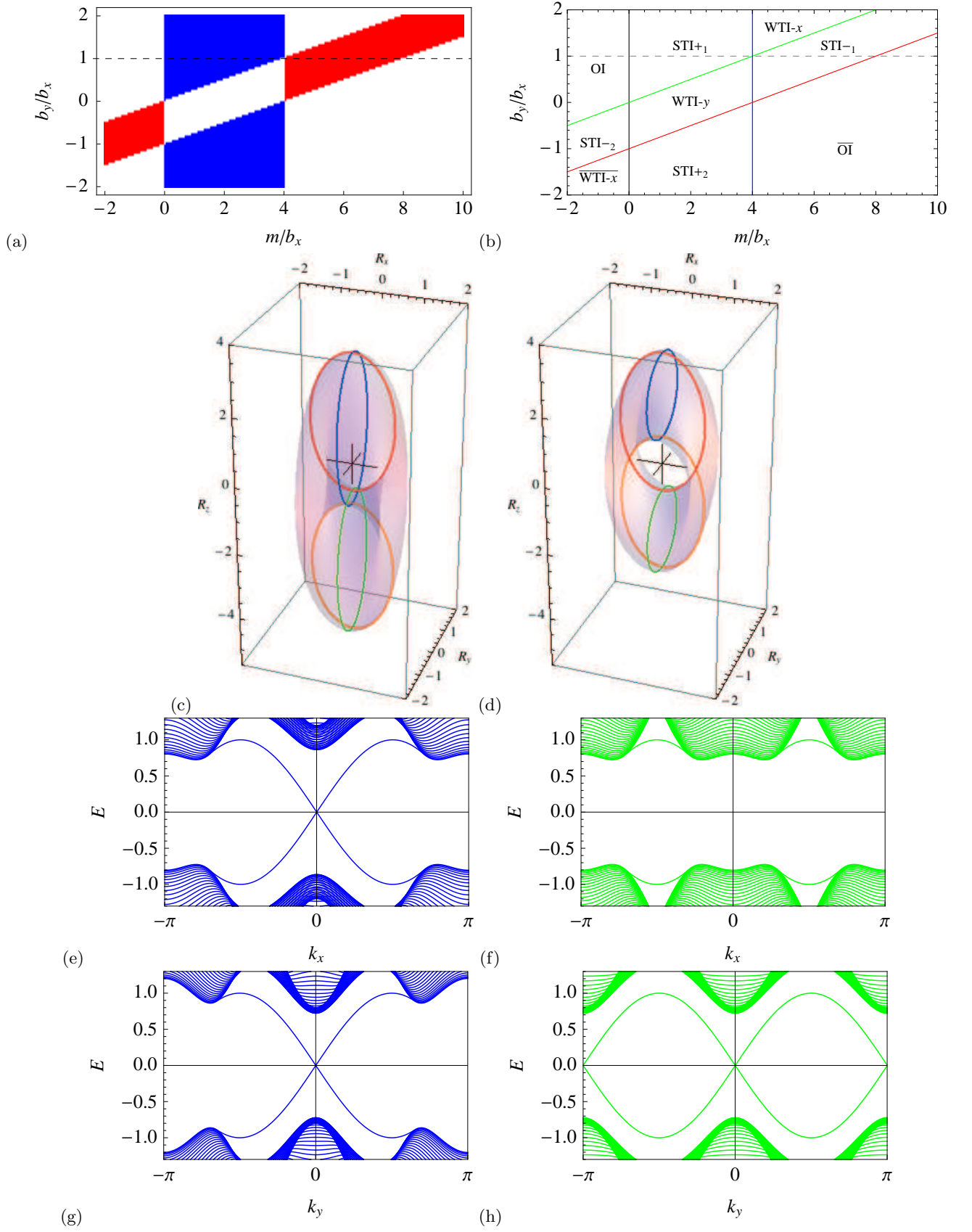


FIG. 1: The anisotropic Wilson-Dirac model. (a) Phase diagram determined by numerical estimation of the bulk Chern number \mathcal{N} . $b_x = 1.0, t = 1.0$. (b) Phase boundaries determined by i) the existence vs. absence of edge modes, and ii) closing of the bulk energy gap at the four symmetric points: $\mathbf{k} = (0, 0), (\pi, 0), (0, \pi)$ and (π, π) . For each phase boundary, we have checked that the two conditions i) and ii) coincide. The bulk band indices [see Eq. (I)] are also indicated in the figure. (c), (d) Graphic representation of the closed surface $\mathcal{R}[T^2]$ and the closed loops $\mathcal{R}[C_{k_y}[0]]$ (blue), $\mathcal{R}[C_{k_y}[\pi]]$ (green), $\mathcal{R}[C_{k_x}[0]]$ (red), $\mathcal{R}[C_{k_x}[\pi]]$ (orange) (see Sec. III). (e-h) Edge (and bulk) spectra in different topological phases: STI+1 [panels (e), (g)], WTI-y [panels (f), (h)], and in two different types of ribbon geometries: x -oriented [panels (e), (f)], y -oriented [panels (g), (h)].

II. MODELS AND THEIR BASIC PROPERTIES

To realize a topologically nontrivial insulating phase on a lattice in crystalline solids, let us consider the following variation of the Wilson-Dirac type Hamiltonian.^{23–25} The model is defined on a 2D square lattice in the tight-binding approximation as

$$H = \sum_{\mathbf{r}} \sum_{\mu=x,y} \left(|\mathbf{r}\rangle \Gamma_{\mu} \langle \mathbf{r} + \hat{\mu}| + |\mathbf{r} + \hat{\mu}\rangle \Gamma_{\mu}^{\dagger} \langle \mathbf{r}| \right) + \sum_{\mathbf{r}} |\mathbf{r}\rangle V(\mathbf{r}) \langle \mathbf{r}| \quad (1)$$

where

$$V(\mathbf{r}) = [m - 2(b_x + b_y)] \sigma_z, \quad \Gamma_{\mu} = -\frac{it_{\mu}}{2} \sigma_{\mu} + b_{\mu} \sigma_z \quad (2)$$

are, respectively, on-site potential and nearest neighbor hopping terms. Let us first assume that the Wilson terms b_{μ} and the strength of hopping t_{μ} are both isotropic:

$$b_x = b_y \equiv b, \quad t_x = t_y \equiv t. \quad (3)$$

Then, in (crystal) momentum space, and in the long-wavelength approximation the Hamiltonian specified by Eqs. (1) and (2) reproduces the standard Wilson-Dirac form:

$$h(\mathbf{k}) = t(k_x \sigma_x + k_y \sigma_y) + (m - b\mathbf{k}^2) \sigma_z. \quad (4)$$

Either on each site \mathbf{r} in real space, or at a given momentum \mathbf{k} in the BZ, this model Hamiltonian takes a 2×2 minimal matrixial form.

On one hand, the matrix nature of the Hamiltonian stems from an orbital degree of freedom inherent to its construction. In the presence of real spin degrees of freedom possibly with the presence of time reversal symmetry a similar minimal representation of the effective Hamiltonian becomes 4×4 .²³ On the other hand, if the matrix nature is due to the particle-hole symmetry of Bogoliubov-de Gennes type, this Hamiltonian can be regarded as that for $p + ip$ superconductors. In this case, the hopping term and the Wilson term in Eqs. (2) or (4) become the pairing gap and the kinetic term, respectively. More rigorous equivalence is summarised in Appendix A.

As demonstrated in various contexts this isotropic version of the Wilson-Dirac model exhibits only the strong topological (STI) and the ordinary (OI) insulating phases, which realize in regimes: either (i) $0 < m/b < 4$ or (ii) $4 < m/b < 8$ (for STI), and $m/b < 0$ or $8 < m/b$ (for OI). In between there is a room for realizing a gapless Dirac semimetallic state in the clean limit.^{26,27}

Since one of our purposes of the present paper is to study the variety of topological phases the Wilson-Dirac model has, especially to quantify 2D weak topological insulating (WTI) phases, we consider in the remainder of the paper, three typical variation of this uniform limit. We first allow the Wilson term b_{μ} to be *anisotropic*. Secondly, we extend the model to include *next nearest*

neighbor hopping terms.²⁸ Finally we consider a *superlattice* generalization of the the original Hamiltonian [Eq. (1) and (2)].

TABLE I: List of Δ 's [for its definition, see Eq. (8)] in different topological phases

	$\begin{bmatrix} + & - \\ - & + \end{bmatrix}$		$\begin{bmatrix} - & + \\ + & - \end{bmatrix}$	
	OI		$\overline{\text{OI}}$	
WTI	$\begin{bmatrix} + & - \\ + & - \end{bmatrix}$		$\begin{bmatrix} - & + \\ - & + \end{bmatrix}$	
	WTI- x		$\overline{\text{WTI-}x}$	WTI- y
$\text{STI}_{\mathcal{N}=\pm 1}$	$\begin{bmatrix} + & - \\ + & + \end{bmatrix}$		$\begin{bmatrix} - & + \\ + & + \end{bmatrix}$	$\begin{bmatrix} - & - \\ + & - \end{bmatrix}$
	STI $_{+1}$		STI $_{+2}$	STI $_{-1}$ STI $_{-2}$
$\text{STI}_{\mathcal{N}=\pm 2}$	$\begin{bmatrix} + & + \\ + & + \end{bmatrix}$		$\begin{bmatrix} - & - \\ - & - \end{bmatrix}$	
	STI $_{\mathcal{N}=+2}$		STI $_{\mathcal{N}=-2}$	

A. Anisotropic Wilson-Dirac model

Let us consider the case of $b_x \neq b_y$. This leads to a visible increase in the diversity of topological phases [see FIG. 1 (a)]. As shown in this phase diagram, topological classification of the system into *nine* different types is no longer simply due to a single combination of parameters, as it was the case in the uniform limit; the single combination was m/b , but a function of *e.g.*, m/b_x and b_y/b_x as is the case in FIG. 1 (a). Two types of STI phases are specified in panel (a): shown either in red or in blue. They correspond to a different (nontrivial) Chern number: $\mathcal{N} = \pm 1$, and can be identified by numerically estimating this number \mathcal{N} . Vanishing of the Chern number \mathcal{N} , on contrary, does not necessarily mean that all of the parameter regions in this category are topologically identical and trivial.

To uncover such topologically non-trivial phases in the $\mathcal{N} = 0$ sector let us introduce the following set of bulk band indices,²⁹ associated with four Dirac points, $\mathbf{k}_D = (0,0), (\pi,0), (0,\pi), (\pi,\pi)$, inherent to the model. Table I lists a composition of such indices in the different topological phases so far identified and named in FIG. 3 and in FIG. 5. Here, in our two band model, the band indices are either $+$ or $-$, which is defined by the sign of the mass terms taking into account the sign of the γ -matrices in the continuum limit in such a way that each index gives the Chern number $\delta_{\mathbf{k}}/2$.³⁰

The band indices $\delta_{\mathbf{k}}$ can be determined in the following way. The tight-binding Hamiltonian Eq.(1) and (2) can

be rewritten in momentum space as

$$H(\mathbf{k}) = t_x \sin k_x \sigma_x + t_y \sin k_y \sigma_y + (m - 2b_x(1 - \cos k_x) - 2b_y(1 - \cos k_y))\sigma_z. \quad (5)$$

At the neighborhood of the four Dirac points $\mathbf{k} = \mathbf{k}_D + \mathbf{p}$, Eq. (5) can be expressed as follow,

$$H(\mathbf{k}_D + \mathbf{p}) = \tilde{t}_x p_x \sigma_x + \tilde{t}_y p_y \sigma_y + (\tilde{m} + O(|\mathbf{p}|^2))\sigma_z, \quad (6)$$

by using $\mathbf{k} \cdot \mathbf{p}$ -approximation. The specific values of \tilde{t}_x , \tilde{t}_y and \tilde{m} for each symmetric points \mathbf{k}_D are shown in TABLE II. Then one can define $\delta_{\mathbf{k}}$ such that

$$\delta_{\mathbf{k}} = \text{sgn}[\tilde{t}_x] \text{sgn}[\tilde{t}_y] \text{sgn}[\tilde{m}]. \quad (7)$$

TABLE II: List of \tilde{t}_x , \tilde{t}_y and \tilde{m} at four Dirac points \mathbf{k}_D

\mathbf{k}_D	\tilde{t}_x	\tilde{t}_y	\tilde{m}
(0, 0)	t_x	t_y	m
$(\pi, 0)$	$-t_x$	t_y	$m - 4b_x$
$(0, \pi)$	t_x	$-t_y$	$m - 4b_y$
(π, π)	$-t_x$	$-t_y$	$m - 4b_x - 4b_y$

Let us define the set of four indices at \mathbf{k}_D by

$$\Delta = \begin{bmatrix} \delta_{0,\pi} & \delta_{\pi,\pi} \\ \delta_{0,0} & \delta_{\pi,0} \end{bmatrix}. \quad (8)$$

Then, the four elements of Δ are related to the Chern number \mathcal{N} as

$$\frac{1}{2}\delta_{0,0} + \frac{1}{2}\delta_{\pi,0} + \frac{1}{2}\delta_{0,\pi} + \frac{1}{2}\delta_{\pi,\pi} = \mathcal{N}. \quad (9)$$

In Eq. (9) each of the four elements $(1/2)\delta_{\mathbf{k}} = \pm 1/2$ is a contribution from a Dirac point at $\mathbf{k}_D = \Gamma, X, Y, M$; this is a standard Dirac cone argument for the Chern number. For the Chern numbers of more generic models, see Sec. IV A, in which we show the details of the method of the numerical calculation.

Furthermore, Δ contains more information than the single Chern number, and allow for full classification not only of the OI and STI, but also of a variety of weak TI phases. Namely, from Δ we can know the Berry phases of the continuum Dirac fermions at a given loop in the Brillouin zone. It has been shown that the Berry phase is quantized as 0 or π for the model with chiral symmetry, which implies, respectively, no edge state and an edge state [more precisely, even edge states and odd edge states] at the zero energy if the model has boundaries.^{2131,32} To be more specific, another combination,

$$\frac{\pi}{2}\delta_{k_x,0} + \frac{\pi}{2}\delta_{k_x,\pi} = \mathcal{N}_x(k_x)\pi, \quad (10)$$

yielding a new quantum number (the Berry phase in unit of π) $\mathcal{N}_x(k_x)$ at $k_x = 0$ and at $k_x = \pi$, specifies whether the edge spectrum crosses (if $\mathcal{N}_x \bmod 2 = 1$) [or not (if $\mathcal{N}_x \bmod 2 = 0$)] at this momentum k_x , while a different combination,

$$\frac{\pi}{2}\delta_{0,k_y} + \frac{\pi}{2}\delta_{\pi,k_y} = \mathcal{N}_y(k_y)\pi, \quad (11)$$

leads to still another quantum number $\mathcal{N}_y(k_y)$ [at $k_y = 0$ and at $k_y = \pi$], and determines whether the edge spectrum crosses (if $\mathcal{N}_y \bmod 2 = 1$) [or not (if $\mathcal{N}_y \bmod 2 = 0$)] at the momentum k_y . Eqs. (10), (11) can be regarded as the “weak version” of the standard Dirac cone argument, here applied to the Berry phase. Contribution from an isolated Dirac point to the Berry phase is $\pm\pi/2$ in an appropriate gauge. Here, such contributions from two Dirac points (doublers) on a path in the BZ torus sum up to a quantized Berry phase π ; the value of the Wilson loop (the lattice version of the Berry phase) associated with this path (see Sec. VI for details).

As demonstrated in panel (b) of FIG. 1, the $\mathcal{N} = 0$ sector of panel (a) is indeed divided into five subregions: OI, OI, WTI- x , WTI- x and WTI- y , in which the last three correspond to *weak* topological phases. In the WTI- x and WTI- y phases, two Dirac points (= crossing of the two branches of edge spectrum) appear at $k_{1D} = 0$ and at π on the edge of a ribbon organized in the direction specified by its name, while the spectrum is gapped (no Dirac point) when the ribbon is perpendicular to that direction. In analogy with the weak indices introduced for specifying different WTI phases in 3D,^{29,33–35} the above WTI- x and WTI- y phases may be represented, respectively, by analogous “weak indices” $(\nu_1, \nu_2) = (1, 0)$, and $(\nu_1, \nu_2) = (0, 1)$.

B. Next-nearest neighbor hopping model

Let us then consider a variation with next-nearest neighbor (NNN) hopping:

$$H_{NNN} = \sum_{\mathbf{r}} [|\mathbf{r}\rangle \Gamma_1 \langle \mathbf{r} + \hat{x} + \hat{y}| + |\mathbf{r} + \hat{x} + \hat{y}\rangle \Gamma_1^\dagger \langle \mathbf{r}|] + \sum_{\mathbf{r}} [|\mathbf{r}\rangle \Gamma_2 \langle \mathbf{r} - \hat{x} + \hat{y}| + |\mathbf{r} - \hat{x} + \hat{y}\rangle \Gamma_2^\dagger \langle \mathbf{r}|] + \sum_{\mathbf{r}} [|\mathbf{r}\rangle V_{NNN}(\mathbf{r}) \langle \mathbf{r}|], \quad (12)$$

where

$$\begin{aligned} \Gamma_1 &= \frac{t}{4i}\sigma_x - \frac{t}{4i}\sigma_y + b_{xy}\sigma_z, \\ \Gamma_2 &= \frac{t}{4i}\sigma_x + \frac{t}{4i}\sigma_y + b_{xy}\sigma_z, \\ V_{NNN}(\mathbf{r}) &= -4b_{xy}\sigma_z. \end{aligned} \quad (13)$$

Here, the Wilson terms are assumed to be isotropic : $b_x = b_y = b$. This case is of interest, since in Ref.²⁸ it

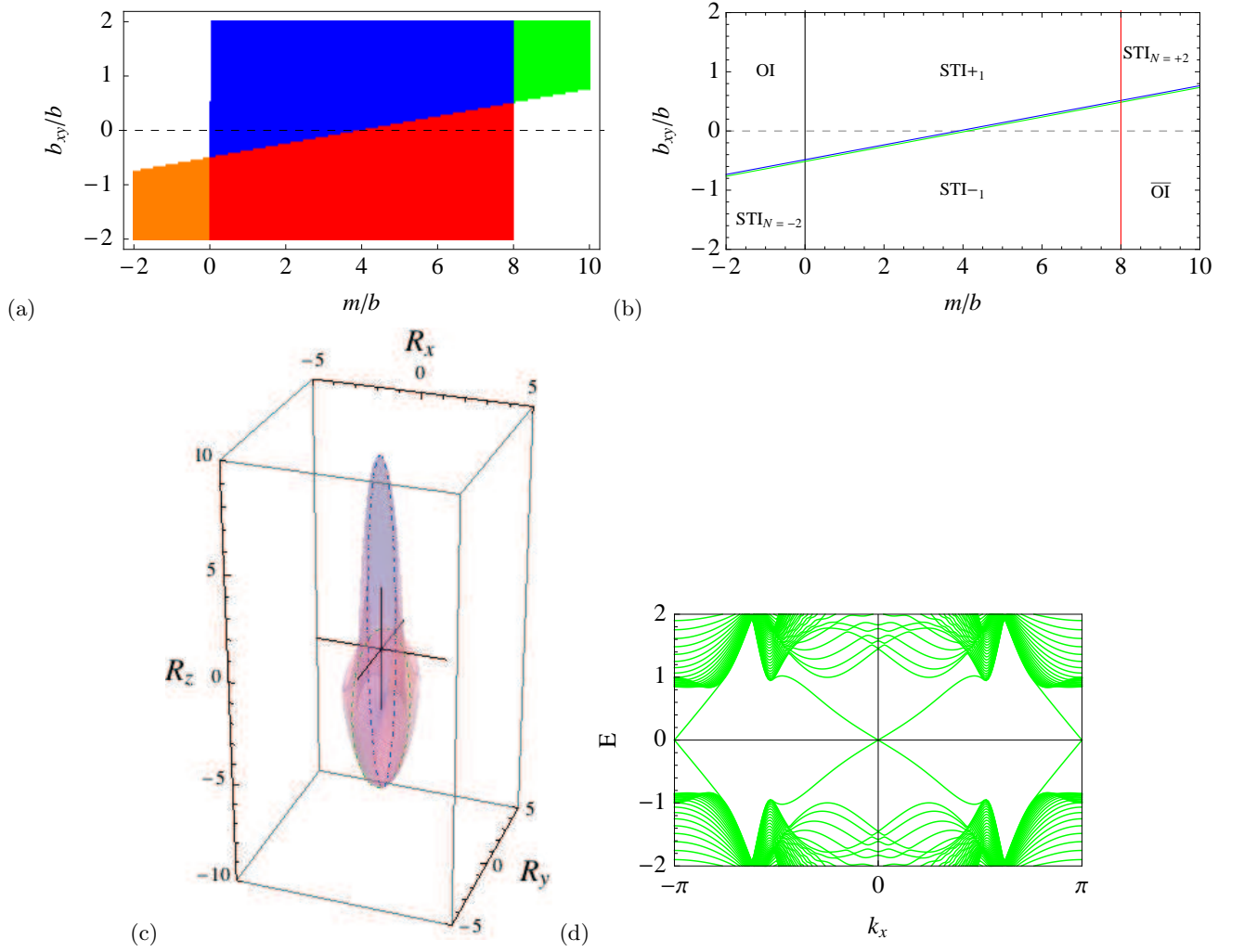


FIG. 2: NNN hopping model. (a) Phase diagram determined by numerical estimation of the Chern number \mathcal{N} . Parameter regions corresponding to different \mathcal{N} are specified by different colors; painted, respectively, in blue ($\mathcal{N} = 1$), red ($\mathcal{N} = -1$), green ($\mathcal{N} = 2$), orange ($\mathcal{N} = -2$), and white ($\mathcal{N} = 0$). $b = 1.0, t = 1.0$. (b) Phase boundaries, and the bulk band indices. (c) Graphic representation of the closed surface $\mathcal{R}[T^2]$ and the closed loops $\mathcal{R}[C_{k_y}[0]]$ (blue), $\mathcal{R}[C_{k_y}[\pi]]$ (green), $\mathcal{R}[C_{k_x}[0]]$ (red), $\mathcal{R}[C_{k_x}[\pi]]$ (orange) in the $STI_{\mathcal{N}=2}$ phase. $m = 9.0, b_{xy} = 1.5$. (d) The edge spectrum in the $STI_{\mathcal{N}=2}$ phase. Here, the ribbon is extended along the x -axis, while the same spectrum is obtained for a ribbon along the y -axis.

was proposed that the model exhibits also weak phases, but with edge modes that appear both in the x - and y -directions.

Different topological phases of this NNN hopping model are shown in FIG. 2. As demonstrated in the figure, they can be characterized either by the Chern number [see panel (a)], or by the bulk band indices [see panel (b)]. In contrast to the previous case of the anisotropic hopping model, the NNN hopping model exhibits strong phases with Chern number $\mathcal{N} = \pm 2$ [$STI_{\mathcal{N}=2}$ and $STI_{\mathcal{N}=-2}$ phases in panel (b); see also the corresponding parameter regions in panel (a)]. In the ribbon geometry, either in the x - or in the y -direction, the model exhibits two Dirac cones at $k_x = 0, \pi$ or at $k_y = 0, \pi$ [see panel (d)]. Yet, in contradiction with what is asserted in Ref.²⁸, these two Dirac cones stem from the Chern number $\mathcal{N} = \pm 2$, and

the two regions should be regraded as STI phases. In WTI phases of the anisotropic model the two low-lying edge modes at $k = 0$ and $k = \pi$ are counter-propagating, while here, the edge modes are co-propagating, in consistency with different Chern numbers in the two phases.

C. The superlattice model

The final and the most focused variation, as far as this paper is concerned, of the original model [Eq. (1) and (2)] is the superlattice generalization. Here, we choose to allow the (half) band gap, the parameter m that appear in definition of the on-site potential term V in Eq. (2) to become \mathbf{r} -dependent: $m \rightarrow m(\mathbf{r})$; V becomes also

\mathbf{r} -dependent:

$$V \rightarrow V(\mathbf{r}) = [m(\mathbf{r}) - 4b] \sigma_z, \quad (14)$$

and alternates such that

$$m(\mathbf{r}) = \begin{cases} m_A & (x \bmod q = 1, 2, \dots, q-1) \\ m_B & (x \bmod q = 0) \end{cases}, \quad (15)$$

i.e., for sake of the simplicity, we consider the case of such patterns that vary as ABAB \cdots ($m = m_A, m_B, m_A, m_B, \dots$ on rows $x = 1, 2, 3, 4, \dots$) or AABAAB \cdots ($m = m_A, m_A, m_B, m_A, m_A, m_B, \dots$ on rows $x = 1, 2, 3, 4, 5, 6, \dots$) on subsequent rows on the square lattice. The spatial profile of the change of this mass term is chosen to be a vertical stripe (a one-dimensional periodic pattern, periodic in the x -direction, while translationally invariant in the y -direction), modeling a semiconductor superlattice, recently fabricated as a three-dimensional layered system.^{20,36} The advantage of the superlattice construction is that one can, in principle, arbitrarily change and control the profile of this pattern.

It is instructive to represent the tight-binding Hamiltonian, now specified by Eqs. (1), (2), (14) and (15) in Fourier space. For ABAB \cdots type superlattice, this becomes

$$\mathcal{H}(\mathbf{k}) = \begin{pmatrix} \Lambda_A & \Gamma_x + e^{-ik_x} \Gamma_x^\dagger \\ \Gamma_x^\dagger + e^{ik_x} \Gamma_x & \Lambda_B \end{pmatrix}, \quad (16)$$

while in the case of AABAAB \cdots like pattern the same Fourier space Hamiltonian is represented by

$$\mathcal{H}(\mathbf{k}) = \begin{pmatrix} \Lambda_A & \Gamma_x & e^{-ik_x} \Gamma_x^\dagger \\ \Gamma_x^\dagger & \Lambda_A & \Gamma_x \\ e^{ik_x} \Gamma_x & \Gamma_x^\dagger & \Lambda_B \end{pmatrix}, \quad (17)$$

where $\Lambda_\alpha = [m_\alpha - 2b(2 - \cos k_y)]\sigma_z + t \sin k_y \sigma_y$, ($\alpha = A, B$). Reflecting the real space periodicity q (e.g., $q = 2$ for the ABAB, and $q = 3$ for AABAAB superlattices), the Fourier space Hamiltonian $\mathcal{H}(\mathbf{k})$ is represented by a $q \times q$ block matrix. The periodicity q and magnitudes of the band gap m_A, m_B, \dots are control parameters at the level of experimental condition and material design. As demonstrated in FIG. 3 changing these parameters, we can generate different topological phases. One of our eventual purposes would be, by controlling them, to switch on and off topologically protected 1D channels in nanocircuits embedded in a system of topological insulator superlattices.⁶

III. A GRAPHIC CLASSIFICATION OF WEAK AND STRONG TOPOLOGICAL PHASES: CASE OF THE 2×2 MATRIX MODELS

In Sec. II-A and II-B, which correspond to FIG. 1, FIG. 2, we have introduced (i) anisotropic, and (ii) NNN hopping models, and classified their topological phases. We have seen the following:

1. Topological classification of the system into different Chern numbers $\mathcal{N} = 0, \pm 1$ [$\mathcal{N} = \pm 1$ corresponds to STI phases, while $\mathcal{N} = 0$ corresponds either to OI or WTI phase.] is safely applicable to these models.
2. Further classification of the $\mathcal{N} = 0$ sector into OI and different WTI phases is possible using the bulk band indices introduced in Eq. (8).
3. In the NNN hopping model, there appear $\text{STI}_{\mathcal{N}=2}$ and $\text{STI}_{\mathcal{N}=-2}$ phases with a nontrivial Chern number $\mathcal{N} = \pm 2$.

Here, we first introduce a graphic representation of the above classification by the Chern number [point (1) above], introduced in Refs.^{37,38}, which allows for characterization of the *strong* properties, then extends this idea to be applicable to characterize *weak* properties.

A. A graphic characterization of the strong topological properties

Let us focus on a mapping \mathcal{R} from the BZ torus (T^2): a 2D space spanned by $\mathbf{k} = (k_x, k_y)$ to a closed surface $\mathcal{R}[T^2]$ that appears as a trajectory of a 3D vector $\mathbf{R}(\mathbf{k})$ defined in a 3D parameter space: $\mathbf{R} = (R_x, R_y, R_z)$. Here, the mapping \mathbf{R} encodes information on the Wilson-Dirac Hamiltonian, [specified by Eqs. (1), (2), in case (i), while Eqs. (1), (2) and (12), in case (ii)] represented in momentum space as

$$h(\mathbf{k}) = \mathbf{R}(\mathbf{k}) \cdot \boldsymbol{\sigma} = R_x(\mathbf{k})\sigma_x + R_y(\mathbf{k})\sigma_y + R_z(\mathbf{k})\sigma_z. \quad (18)$$

As shown in Refs.^{37,38}, information on the bulk Chern number \mathcal{N} , which is defined as the value of Berry curvature integrated over the 2D BZ torus, can be transcribed, in the 3D \mathbf{R} -parameter space, into the number of times $\mathcal{N}_{\text{covering}}$ in which the origin in the target \mathbf{R} -space is covered by the closed surface $\mathcal{R}[T^2]$ when \mathbf{k} sweeps once around the entire BZ torus. Indeed, one can verify $\mathcal{N} = -\mathcal{N}_{\text{covering}}$. This signifies as shown in the two panels: (c) vs. (d) of FIG. 1 [parameters corresponding to (c) represent an STI, while those of (d) represent a WTI phase], one can tell what the Chern number of the system is by investigating the global behavior of the closed surface $\mathcal{R}[T^2]$ with respect to the origin in the 3D \mathbf{R} -parameter space. In the $\text{STI}_{\mathcal{N}=2}$ region of the NNN hopping model [see FIG. 2 panel (c)] the origin is covered twice by $\mathcal{R}[T^2]$.

B. A new classification scheme for identifying WTI phases

To extract the Berry phase characterizing the *weak* topological properties from the same mapping \mathcal{R} , let us consider a straight line $\mathcal{C}_{k_y}[k_x]$ or $\mathcal{C}_{k_x}[k_y]$ in the BZ, at either k_x (for $\mathcal{C} = \mathcal{C}_{k_y}$) or k_y (for $\mathcal{C} = \mathcal{C}_{k_x}$) fixed, which

represents a closed loop on the BZ torus. To characterize the weak properties in our models, we will be specifically concerned about how \mathcal{R} maps these closed loops on the BZ torus; especially, $\mathcal{C}_{k_y}[k_x]$ at $k_x = 0$ and π , as well as $\mathcal{C}_{k_x}[k_y]$ at $k_y = 0$ and π . Generally, mapping of these closed loops represents also a closed loop in the \mathbf{R} -space. Note also that these loops in the target space: $\mathcal{R}[\mathcal{C}_{k_y}[k_x = 0]]$, $\mathcal{R}[\mathcal{C}_{k_y}[k_x = \pi]]$, $\mathcal{R}[\mathcal{C}_{k_x}[k_y = 0]]$ and $\mathcal{R}[\mathcal{C}_{k_x}[k_y = \pi]]$ are not only on $\mathcal{R}[T^2]$, but always on a plane that includes the origin in the \mathbf{R} -space. This implies that on the given loop, the model has chiral symmetry, and hence, the Berry phase should be quantized, as mentioned in Sec. II A.²¹ If $\mathcal{R}[\mathcal{C}[k_\mu]]$ encircles the origin, then the two branches of the corresponding edge spectrum in a ribbon geometry laid in the μ -direction cross at this value of k_μ , while if it does not encircle the origin, the spectrum is generally gapped at the same k_μ . Thus, information on the global property of $\mathcal{R}[T^2]$ and the four closed loops: $\mathcal{R}[\mathcal{C}[k_\mu]]$ at four Dirac points in the BZ with respect to the origin fully specify the weak and strong topological properties of the system.

In FIG. 1 panel (c) represents such an information in a WTI- y phase with “weak indices” $\nu = (\nu_1, \nu_2) = (1, 0)$ [indicating that an edge $\perp \nu$ is a dark surface⁶ without surface modes] so that both $\mathcal{R}[\mathcal{C}_{k_x}[k_y = 0]]$ and $\mathcal{R}[\mathcal{C}_{k_x}[k_y = \pi]]$ encircle the origin in the \mathbf{R} -space, while neither $\mathcal{R}[\mathcal{C}_{k_y}[k_x = 0]]$ nor $\mathcal{R}[\mathcal{C}_{k_y}[k_x = \pi]]$ winds the origin.

On contrary, panel (c) in FIG. 2 represents the same kind of information in the STI $_{N=2}$ phase; there, all the four loops encircle the origin in the \mathbf{R} -space.

IV. PHASE DIAGRAM OF THE SUPERLATTICE MODEL

The above classification scheme outlined in Sec. III is no longer applicable to the superlattice model, since the superlattice structure introduces supplementary matrix nature to the model (in addition to the original 2×2 structure) which is antithetical to the manifold scheme. Yet, the two dimensionality of the model allows, at least, for calculation of the Chern number that can be used for classifying topologically nontrivial phases. Here, applying the prescription of Ref.³⁹ to the superlattice system, we estimate numerically the Chern number at different points in the (m_A, m_B) -plane for a given strength of hopping t .

A. Calculation of the Chern number in multiband systems and in the discretized BZ

For the multi-band systems, we calculate the Berry connection and curvature on the discretized Brillouin zone developed in Ref.³⁹. On the square lattice composed of the set of discretized momentum k_ℓ on the Brillouin

zone $[0, 2\pi] \otimes [0, 2\pi]$ defined as

$$k_\ell = \left(\frac{2\pi j_x}{L_x}, \frac{2\pi j_y}{L_y} \right), \quad (19)$$

where $j_\mu = 0, 1, \dots, L_\mu$, the Berry connection is defined by the link variable

$$U_\mu(k_\ell) = \det \psi^\dagger(k_\ell) \psi(k_\ell + \hat{\mu}), \quad (20)$$

where $\hat{\mu}$ stands for the unit lattice vector to k_μ direction, $\hat{\mu} = 2\pi/L_\mu$. Manifestly gauge invariant Berry curvature is then given by the plaquette variable

$$F_{xy}(k_\ell) = \text{Im} \ln [U_x(k_\ell) U_y(k_\ell + \hat{x}) U_x^{-1}(k_\ell + \hat{y}) U_y^{-1}(k_\ell)], \quad (21)$$

where the branch of \ln is restricted to $F \in (-\pi, \pi)$. A lattice analogue of the vortices is defined as follows. Let $A_\mu(k_\ell)$ be a gauge potential defined by

$$A_\mu(k_\ell) = \text{Im} \ln U_\mu(k_\ell), \quad (22)$$

where the branch is also defined by $A_\mu \in (-\pi, \pi)$. We can show

$$F_{xy}(k_\ell) = \Delta_x A_y(k_\ell) - \Delta_y A_x(k_\ell) + 2\pi n_{xy}(k_\ell), \quad (23)$$

where Δ_μ is the forward difference operator, and $n_{xy}(k_\ell)$ is a local *integer* field taking $|n_{xy}| \leq 2$. This n -field can be regarded as the vortices on the lattice. The Chern number is given by

$$\mathcal{N} = \frac{1}{2\pi} \sum_{k_\ell} F_{xy}(k_\ell) = \sum_{k_\ell} n_{xy}(k_\ell). \quad (24)$$

B. Phase diagram: specific features

To understand the structure of the phase diagram shown in FIG. 3 it is convenient to first recall what happens on the uniform line: $m_A = m_B$. The uniform limit of the present model is nothing but “one half”, say, the spin-up part of the BHZ model²³. Also, this occurs naturally on a diagonal line $m_A = m_B$ in phase diagrams of FIG. 3. In the uniform limit, there appear three different topological phases, *i.e.*, one trivial or ordinary (OI phase), and two (strong) topological insulator (quantum anomalous Hall) phases with a protected gapless edge mode propagating either in the clockwise (STI+ phase in our definition) or in the anti-clockwise (STI- phase) direction.

Away from the uniform limit, it is convenient to consider a phase diagram in the (m_A, m_B) -plane at fixed hopping t . At each point on this plane we estimate numerically the Chern number to determine which of the three topological classes (OI, STI+ and STI-) the system belongs to. The resulting phase diagram is shown in FIG. 3 [panels (a) and (d)].

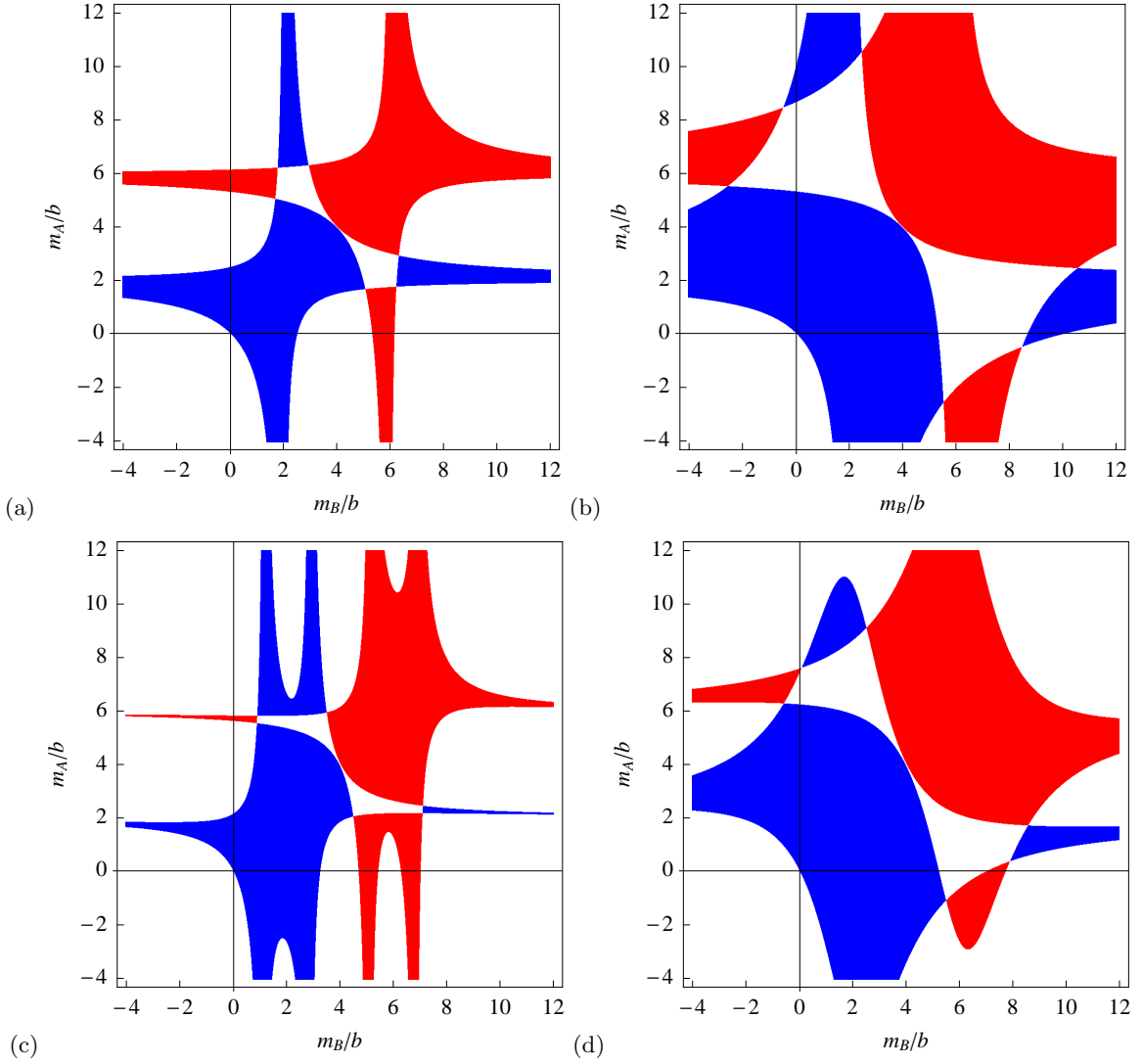


FIG. 3: Phase diagram of the superlattice model determined by numerical estimation of the Chern number \mathcal{N} . Parameter regions represented by different colors correspond to $\mathcal{N} = 1$ (blue), $\mathcal{N} = -1$ (red), and $\mathcal{N} = 0$ (white). (a), (b): case of the ABAB... like pattern. (c), (d): *ibid.*, AABAAB... type case. $b = 1.0, t = 1.0$ [panels (a), (c)], $b = 1.0, t = 4.0$ [panels (b), (d)].

In the phase diagrams shown in FIG. 3 STI+ and STI- phases can be understood as a natural extension of their counterparts in the uniform limit. Yet, as contrasted in panels (a) vs. (b), and (c) vs. (d) of FIG. 3 the location of the phase boundaries changes drastically as a function of the strength of hopping. This is quite contrasting to the uniform limit, and to the previous two cases treated so far, *i.e.*, (i) the anisotropic hopping, and (ii) the next-nearest neighbor hopping cases. Here, as shown in FIG. 3 and in contrast to the cases (i) and (ii), the phase boundaries in the (m_A, m_B) -plane are not given by simple straight lines, and also functions of the hopping t . Naturally, the location of the phase boundaries correspond to the closing of the bulk energy gap triggered by the condition $\det H = 0$. In the present realization of the superlattice pattern, symmetries of the model allows for closing of the bulk energy gap at the

four Dirac points: $(k_x, k_y) = (0, 0), (\pi, 0), (0, \pi), (\pi, \pi)$. Thus, as shown in FIG. 5 the phase boundaries of FIG. 3 correspond exactly to the location of gap closing at these four symmetric points. For this reason the location of the phase boundaries of FIG. 3 can be determined analytically (see Sec. V).

So far we have focused on the regions of the phase diagram (such as the ones in FIG. 3) painted either in blue or in red, corresponding to regions of non-trivial Chern number $\mathcal{N} = \pm 1$. Let us focus on the part in which these blue and red regions are extended and then "overlap". In this viewpoint the overlap of the two nontrivial regions (*i.e.*, the region corresponding to parts named "WTI-y" in FIG. 5) is a trivial region with a vanishing Chern number $\mathcal{N} = 0$ (unpainted, or painted in white). It looks as if there is a color mixture rule such that blue+red=white, or simply the Chern numbers add to each other. The su-

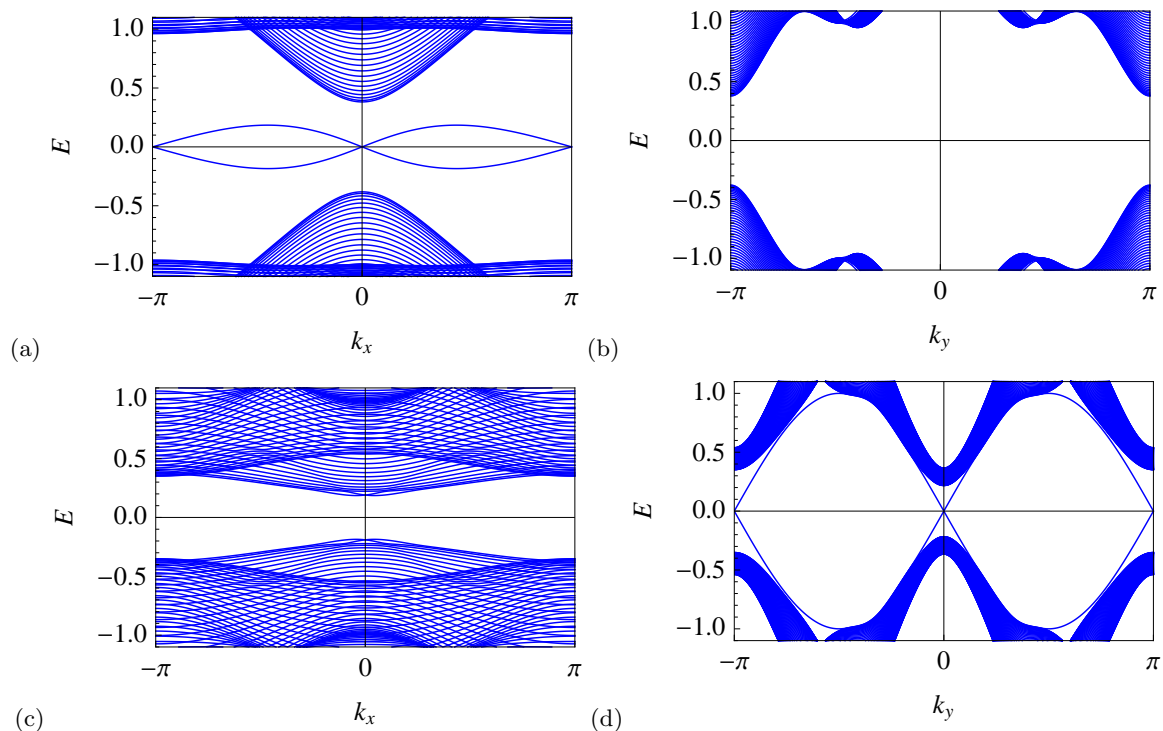


FIG. 4: Energy spectrum in the ribbon geometry. The superlattice is AABAAB \dots type. The system is in the WTI- x phase in panels (a), (b), while it is in the WTI- y phase in panels (c), (d). The ribbon is extended along x -axis in panels (a), (c), while the same is along the y -axis in panels (b), (d).

perlattice composed of alternating stripes with a Chern numbers $\mathcal{N} = 1$ and $\mathcal{N} = -1$, gives rise to a phase with $\mathcal{N} = 0$. However, as implied by its name, the WTI- y phase is not actually topologically trivial, but exhibits protected gapless edge states in a finite geometry. This can be explicitly verified by numerical diagonalization of the tight-binding Hamiltonian in systems with an edge or edges. The spectrum of such edge modes is shown in FIG. 4. Here, we have employed the ribbon geometry (a system with one periodic and one open boundary condition) so that we can distinguish cases in which the edges are either parallel or perpendicular to the superlattice structure.

Naturally, WTI is an abbreviation of the weak topological insulator. We call this phase “weak”, because there are two “Dirac cones” on a surface, say, in a ribbon geometry. Here, what we mean by a Dirac cone is a crossing of the two branches of the edge state, one localized at the left, and the other at the right edge of the ribbon. In the weak phase, this crossing occurs at two points of the new one-dimensional Brillouin zone, *e.g.* $k_y \in [-\pi, \pi]$, and it occurs actually at the two points of the BZ, $k_y = 0$ and at $k_y = \pi$. WTI-“ y ”, because the protected edge states appear only in the ribbon organized in the y -direction.

As demonstrated in FIG. 4, this nontrivial phase with a vanishing Chern number $\mathcal{N} = 0$ exhibits protected gapless states depending on whether the edges are parallel or perpendicular to the superlattice. A similar phenomenon is known and considered to be a characteristic feature of

the more generic 3D WTI phases.

Another example of such a nontrivial weak phase can be found in some of the unpainted fragments of the $\mathcal{N} = 0$ regions in FIG. 3, which are named in FIG. 5 the “WTI- x phase”. As suggested in its name, a pair of protected edge states appear in this phase in a ribbon laid in the x -direction.

V. BULK-EDGE CORRESPONDENCE IN THE SUPERLATTICE MODEL

We have so far seen different topological phases in the superlattice model, and their phase boundaries from two different points of view: one from the Chern number in the bulk, the other from existence vs. absence of edge states. There is, indeed, a one-to-one correspondence between the two viewpoints. Existence of such a correspondence is sometimes regarded as a defining property of the topologically nontrivial system. Here, in this section we make more explicit the nature of this bulk-edge correspondence in the present superlattice model.

A. Bulk-edge correspondence from the viewpoint of bulk band indices

Let us focus on the phase boundaries between different topological phases shown in FIG. 5, and marked by

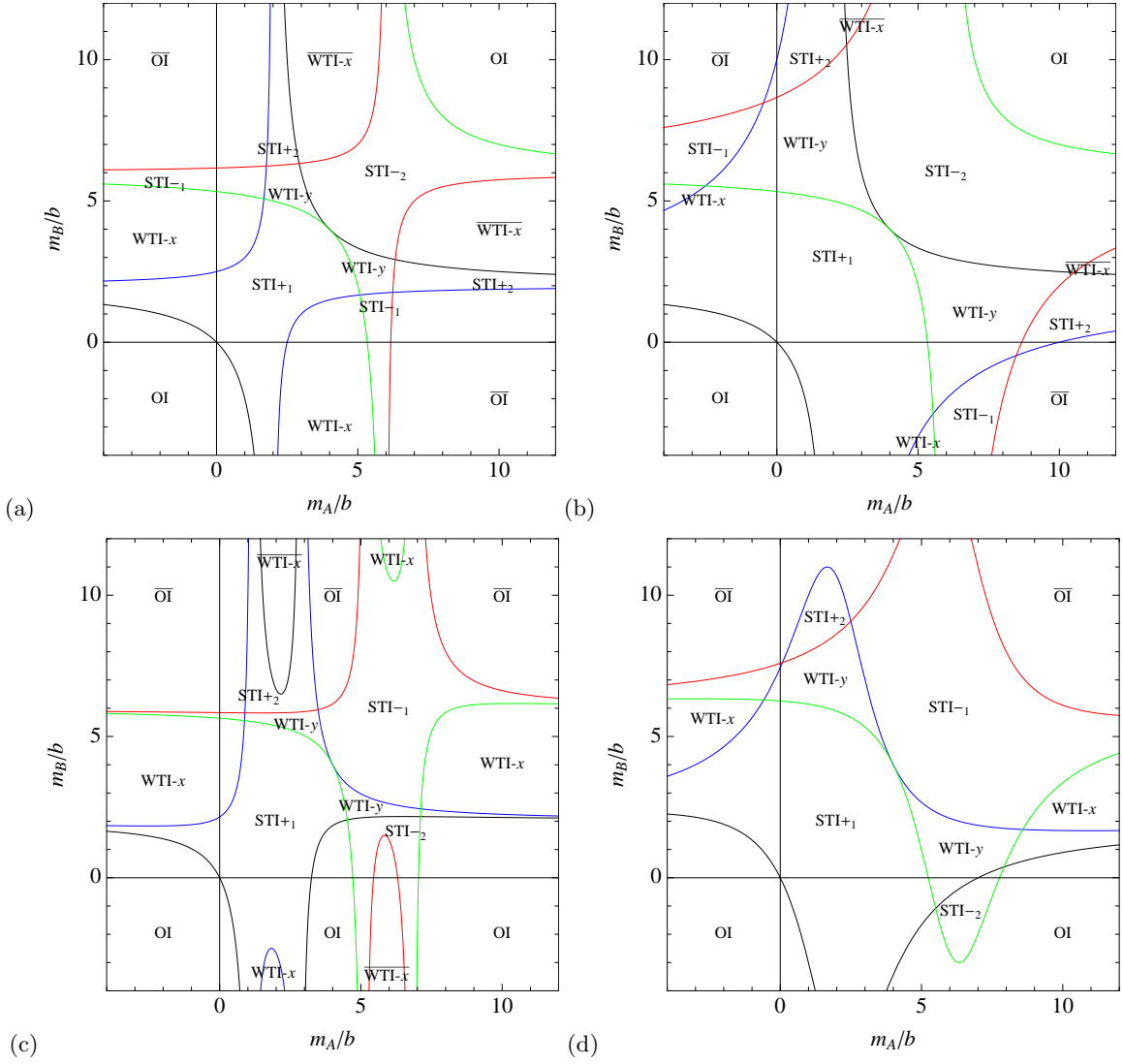


FIG. 5: (Color online) Phase boundaries between and bulk band indices in different topological phases. Panels (a) and (b): cases of the ABAB... type pattern. Panels (c) and (d): cases of the AABAAB... type pattern. Other parameters are set the same as in the corresponding panel in FIG. 3. The phase boundaries are determined by tracing the zeros of $\det H$ at the four symmetric \mathbf{k} -points in the BZ (see the main text). Different colors correspond to zeros of $\det H$ at $(0,0)$ (black), $(\pi,0)$ (blue), $(0,\pi)$ (green) and (π,π) (red).

colored lines. They are colored in four colors in accordance with the number of the Dirac \mathbf{k} -points in the (first) BZ. Each phase boundary is a trajectory of the zeros of $\det H$ at such \mathbf{k} -points. Therefore, there are four different types of phase boundaries, each corresponding to a specific color as indicated in the caption of FIG. 5. Then, comparing FIG. 5 and Table I, one can empirically verify the following (very important) observation: *if one crosses such a phase boundary corresponding to gap closing at a given momentum \mathbf{k} , then the corresponding element of Δ , introduced in Eq. (8) and listed in Table I, alters (its sign) on the opposing sides the phase boundary.*

This observation combined with the assertions associated with Eqs. (10) and (11) [on the (co)relation between the appearance of edge modes and the value of quan-

tum numbers \mathcal{N}_x and \mathcal{N}_y] signifies that such a “skeleton” phase diagram as shown in FIG. 5, determined simply by the trajectory of the gap closing in the parameter space at discrete Dirac points in the BZ, contain a *full* topological information. That is to say, one can fully tell from it whether, where and under what conditions *i.e.*, in which type of the ribbon geometry (x -oriented or y -oriented), the system exhibits protected edge modes. In the remainder of the paper, we further analyze and reveal why the simple set of (band) indices introduced in Eq. (8) acquires such a predictive power.

B. Rationalization by a transfer-matrix type argument

Consider, for simplicity, a ribbon laid in the x -direction, and introduce $\rho = e^{ik_y}$. Focusing on one of the edges of the ribbon, say, the one at $y = 0$, let us ask how the wave function of the edge state penetrates from the boundary $y = 0$ into the bulk region: $y > 0$. To cope with the boundary condition that each component of the wave function vanishes, its scalar part $\psi(y)$ is supposed to vary as⁴⁰

$$\psi(y) = \rho_1^y - \rho_2^y, \quad (25)$$

where ρ 's are different solutions of the eigenvalue equation:

$$\det(\mathcal{H} - \bar{E}) = 0. \quad (26)$$

\bar{E} is the (energy) level of the edge solution, which turns out to be null to be compatible with the boundary condition at $k_x = 0$ or π (at chirally symmetric points). In Eq. (26) $\mathcal{H} = \mathcal{H}(\mathbf{k})$ is regarded as a function of ρ at $k_x = 0$ or π . For the solution (25) to be normalizable in the region: $y > 0$, the condition $|\rho_{1,2}| < 1$ must hold.

Thus, in the present context, verifying the correspondence between the bulk and edge properties has reduced to establishing the equivalence of the following two conditions: (i) the bulk condition: $\det \mathcal{H}(k_x, 0) = 0$ or $\det \mathcal{H}(k_x, \pi) = 0$ and (ii) the edge condition: $|\rho_{1,2}(k_x)| = 1$, at $k_x = 0$ and π . Here, we verify the equivalence of two conditions explicitly on each of the phase boundaries of FIG. 5. At $k_x = 0$ the bulk condition is satisfied, either by $\det H(0, 0) = 0$ on a surface represented by

$$\frac{m_B}{b} = \frac{m_B \left(\frac{m_A}{b}, \frac{t}{b} \right)}{b} = \frac{8 \left(\frac{m_A}{b} \right)^2 - 24 \frac{m_A}{b} - 2 \frac{m_A}{b} \left(\frac{t}{b} \right)^2}{4 \left(\frac{m_A}{b} \right)^2 - 16 \frac{m_A}{b} + \left(\frac{t}{b} \right)^2 + 12}, \quad (27)$$

or by $\det H(0, \pi) = 0$ on a different surface:

$$\frac{m_B}{b} = \frac{24 \left(\frac{m_A}{b} \right)^2 - 280 \frac{m_A}{b} - 2 \frac{m_A}{b} \left(\frac{t}{b} \right)^2 + 12 \left(\frac{t}{b} \right)^2 + 784}{4 \left(\frac{m_A}{b} \right)^2 - 48 \frac{m_A}{b} + \left(\frac{t}{b} \right)^2 + 140} \quad (28)$$

in the $(m_A/b, m_B/b, t/b)$ -space. On these surfaces the edge condition $|\rho(k_x = 0)| = 1$ is satisfied. Cross sections of these surfaces at $t/b = 1.0$ and at $t/b = 4.0$ are shown in FIG. 5 [cross sections of the surface (27) are shown in black, while those of the surface (28) are shown in green].

Similarly, at $k_x = \pi$, the bulk condition is satisfied either by $\det H(\pi, 0) = 0$ on the surface:

$$\frac{m_B}{b} = \frac{8 \left(\frac{m_A}{b} \right)^2 - 24 \frac{m_A}{b} - 2 \frac{m_A}{b} \left(\frac{t}{b} \right)^2 + 12 \left(\frac{t}{b} \right)^2 + 16}{4 \left(\frac{m_A}{b} \right)^2 - 16 \frac{m_A}{b} + \left(\frac{t}{b} \right)^2 + 12} \quad (29)$$

or by $\det H(\pi, \pi) = 0$ on

$$\frac{m_B}{b} = \frac{24 \left(\frac{m_A}{b} \right)^2 - 280 \frac{m_A}{b} - 2 \frac{m_A}{b} \left(\frac{t}{b} \right)^2 + 24 \left(\frac{t}{b} \right)^2 + 800}{4 \left(\frac{m_A}{b} \right)^2 - 48 \frac{m_A}{b} + \left(\frac{t}{b} \right)^2 + 140} \quad (30)$$

On these surfaces the edge condition $|\rho(k_x = \pi)| = 1$ is satisfied. Cross sections of these surfaces at $t/b = 1.0$ and at $t/b = 4.0$ are shown in FIG. 5 [cross sections of the surface (29) are shown in blue, while those of the surface (30) are shown in red].

The fact that (i) the bulk and (ii) the edge conditions are satisfied on the same surfaces given by Eqs. (27), (28), (29) and (30) suggests that an *enhanced* version of the standard bulk-edge correspondence holds here in our system that involves both *strong* and *weak* topological properties. Note that the standard bulk-edge correspondence involves only *strong* properties.

C. The Berry phase on a discretized Brillouin zone

For the multi-band systems, the Berry phase is computed on the discretized Brillouin zone (19) by the use of the link variable defined in Eq. (20) as the so-called Wilson loop such that

$$W[\mathcal{C}_{k_y}[k_x]] = \prod_{j_y=0}^{L_y-1} U_y(k_\ell),$$

$$W[\mathcal{C}_{k_x}[k_y]] = \prod_{j_x=0}^{L_x-1} U_x(k_\ell). \quad (31)$$

We take the $U(1)$ link variables $U_{k_\mu}(k_\ell)$ along a contour \mathcal{C}_{k_μ} . Typically, the contour \mathcal{C}_{k_μ} is chosen to be a (closed) path traversing the entire BZ, “closed” in the viewpoint in which the BZ is regarded as a torus (for the definition of contour \mathcal{C} , see Sec. III B).

The present model, as well as the original two-component Wilson-Dirac model, has particle-hole symmetry, which is enhanced to chiral symmetry at the four Dirac points $\mathbf{k} = (0, 0), (\pi, 0), (0, \pi), (\pi, \pi)$. At these points, $W = 1$ and $W = -1$ correspond to the Berry phase 0 and π , respectively.

TABLE III: Values of the Wilson loop $\text{Im} \ln W[\mathcal{C}[k_\mu]]$ for specific contour $\mathcal{C}[k_\mu]$ at $k_\mu = 0$ and π

	$\mathcal{C}_{k_y}[k_x = 0]$	$\mathcal{C}_{k_y}[k_x = \pi]$	$\mathcal{C}_{k_x}[k_y = 0]$	$\mathcal{C}_{k_x}[k_y = \pi]$
STI+1	π	0	π	0
WTI-x	π	π	0	0
WTI-y	0	0	π	π
OI	0	0	0	0

In FIG. 6 typical examples of the Wilson loop calculated in the STI, WTI and OI phases are shown. In the left and right panels $\text{Im} \ln W[\mathcal{C}_{k_y}[k_x]]$ and $\text{Im} \ln W[\mathcal{C}_{k_x}[k_y]]$ are plotted, respectively. It should be noted that these are defined modulo 2π . The value of $\text{Im} \ln W[\mathcal{C}_{k_y}[k_x]]$ at $k_x = 0, \pi$ is directly related to $\mathcal{N}_x(k_x)$ introduced in Eq. (10), encoding the information on the existence of edge modes in the x -oriented ribbon at $k_x = 0, \pi$, while $\text{Im} \ln W[\mathcal{C}_{k_x}[k_y]]$ at $k_y = 0, \pi$ is a counterpart of $\mathcal{N}_y(k_y)$ given in Eq. (11), encoding the informa-

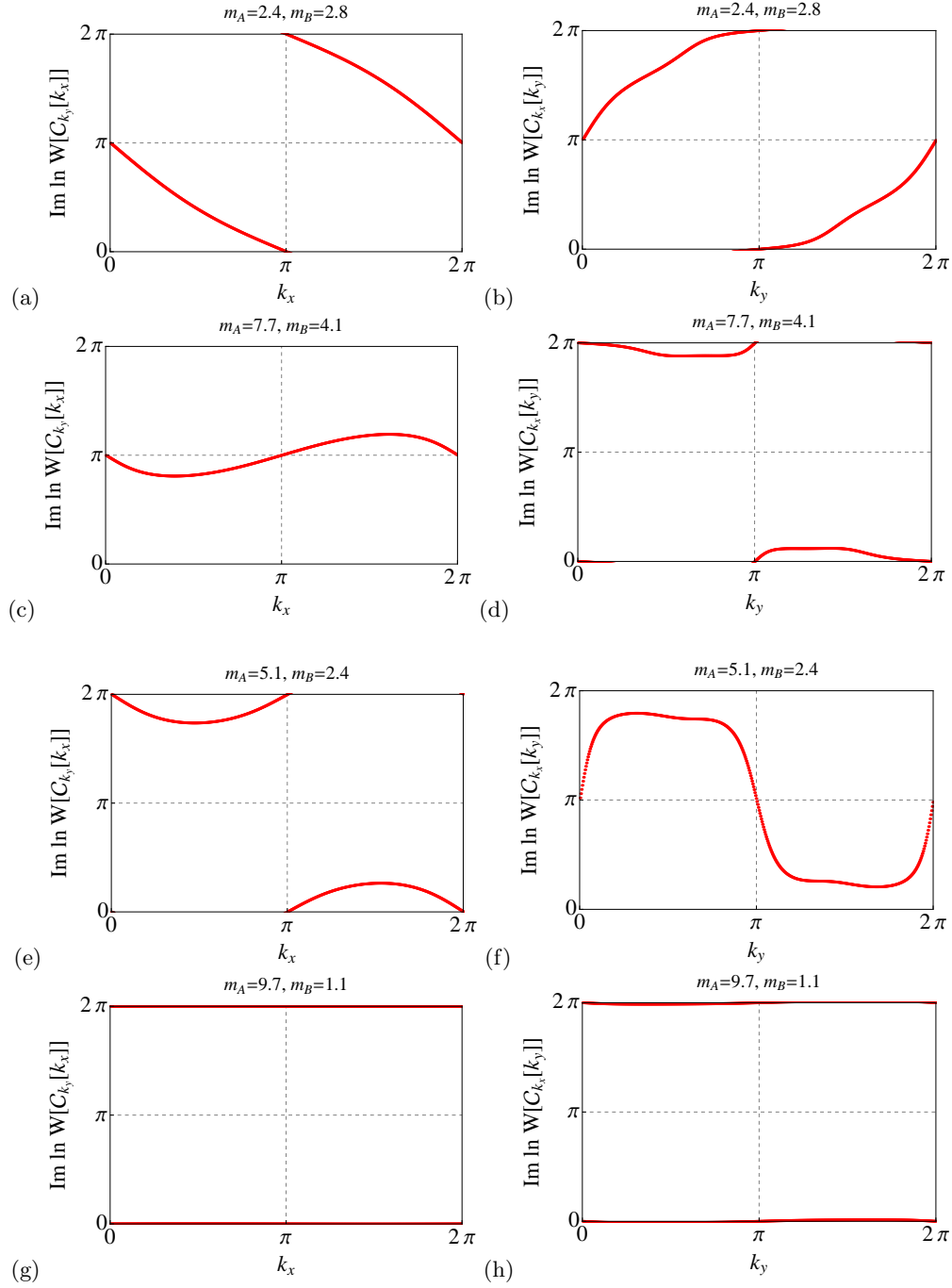


FIG. 6: (Color online) Wilson loop $W[C_{k_y}[k_x]]$ and $W[C_{k_x}[k_y]]$. $W[C_{k_y}[k_x]]$: (a), (c), (e), (g), $W[C_{k_x}[k_y]]$: (b), (d), (f), (h). The system is ...AAB... (a), (b) are case of phase STI+₁ (chern number=+1), (c), (d) are case of phase WTI- y (the edge state appear in the y -direction-edge) and (e), (f) are case of phase WTI- x (the edge state appear in the x -direction-edge), (g), (h) are case of phase OI+.

tion on the y -oriented ribbon (see also Table III). Thus, the quantum numbers \mathcal{N}_x and \mathcal{N}_y are given topological meaning:

$$\text{Im log } W[C_{k_y}[k_x]] = N_x(k_x)\pi + 2\pi n_x, \quad (32)$$

$$\text{Im log } W[C_{k_x}[k_y]] = N_y(k_y)\pi + 2\pi n_y, \quad (33)$$

at $k_x = 0, \pi$ and $k_y = 0, \pi$, where n_x and n_y are arbitrary

integers: $n_x, n_y = 0, \pm 1, \pm 2, \dots$

VI. SUMMARY

Motivated by recent experimental³⁶ realization and subsequent theoretical studies^{20,41} of a superlattice gen-

eralization of the topological insulator, we have developed an extensive theoretical analysis of such a system, using a model defined on a two-dimensional square lattice. First by close diagnosis of the phase diagram composed of various types of topologically different phases, we have established a *strong* correspondence between the bulk and edge properties. The reason why we specify that this correspondence is “strong” was the following. The word, “bulk-edge correspondence”,⁴² one of the key terminologies in the field of topological insulators, signifies an idea that (is believed to) hold in the classification of any type of topological non-triviality. But in the standard use of the terminology in the field, it refers usually to \mathbf{k} -integrated topological features; such as the existence vs. absence of a (pair of) protected gapless bound (localized) state(s) at the edge (of, say, a ribbon geometry) [in the entire spectrum; (entire) = (bulk) + (edge) modes, and *in the entire Brillouin zone* (BZ)], in short, whether there is an edge mode that traverses the entire bulk energy gap, in the context of how this is related to the (non)triviality of the bulk Chern number, or its derivatives (other topological numbers) that is to say, Berry curvature integrated over \mathbf{k} , over the entire BZ. The strong correspondence, here, addressed in this paper deals with \mathbf{k} -selective information, and refers to the so-called “weak” properties. An important by-product of this analysis was the Berry phase $\pi/2$ that has appeared in the sum rule in Eqs. (10), (11).

In the second half of the paper we have proposed and established how the strong correspondence of the bulk and edge properties that plays a central role in the understanding of the phase diagram of various (weak) topological phases is related to the *quantized* Berry phase along (Berry curvature integrated over) a Wilson loop. In the latter terminology, the choice of the loop (the contour of integration) is \mathbf{k} -selective and allows for encoding information on the weak topological properties. Finally, relevance of such “weak” topological properties as discussed in this paper has also been pointed in a slightly different context: *i.e.*, in the study of network models⁴³ and in the context of the entanglement spectrum of topologically nontrivial phases.⁴⁴

Acknowledgments

The authors acknowledge Yositake Takane, Igor Herbut, Fakhere Assaad and Christopher Mudry for useful discussions. This work was supported in part by Grant-in-Aid for Scientific Research from the Japan Society for the Promotion of Science (No. 25400388), and (No. 26247064).

Appendix A: Equivalence to the $p + ip$ superconductors

The Hamiltonian (2) being written by creation and annihilation operators of the Dirac fermion is expressed as

$$\begin{aligned} H = & -\frac{it}{2} \sum_{j,\mu} \left(c_j^\dagger \gamma_\mu c_{j+\hat{\mu}} - h.c. \right) \\ & + \sum_{j,\mu} b_\mu \left(c_j^\dagger \gamma_3 c_{j+\hat{\mu}} + c_{j+\hat{\mu}}^\dagger \gamma_3 c_j - 2c_j^\dagger \gamma_3 c_j \right) \\ & + m \sum_j c_j^\dagger \gamma_3 c_j, \end{aligned} \quad (\text{A1})$$

where $c_j = (c_{j1}, c_{j2})^T$ is the annihilation operator of the Dirac fermion, and we have chosen $\gamma_1 = \sigma_x$, $\gamma_2 = \sigma_z$, and $\gamma_3 = -\sigma_y$. We introduce Majorana fermion operators a_j and b_j such that

$$\begin{pmatrix} c_{j1} \\ c_{j2} \end{pmatrix} = \frac{1}{2} \begin{pmatrix} a_{j1} + ib_{j1} \\ a_{j2} + ib_{j2} \end{pmatrix}, \quad (\text{A2})$$

where $a_{j1,2}^2 = b_{j1,2}^2 = 1$. Then, the Hamiltonian is decoupled; $H = H_a + H_b$, where the Majorana Hamiltonian H_a is defined by⁴⁵

$$\begin{aligned} H_a = & -i\frac{t}{4} \sum_{j,\mu} a_j \gamma_\mu a_{j+\hat{\mu}} + \frac{1}{2} \sum_{j,\mu} b_\mu (a_j \gamma_3 a_{j+\hat{\mu}} - a_j \gamma_3 a_j) \\ & + \frac{m}{4} \sum_j a_j \gamma_3 a_j, \end{aligned} \quad (\text{A3})$$

Here, $a_j = (a_{j1}, a_{j2})^T$ stands for two-component Majorana operator. H_b is the same Hamiltonian but with independent Majorana fermion operator $b_j = (b_{j1}, b_{j2})^T$. Next, we introduce new Dirac fermion operators by recombining the Majorana operators such that $\alpha_j = (a_{j1} + ia_{j2})/2$. Then, H_a becomes

$$\begin{aligned} H_a = & \sum_{j,\mu} \tilde{t}_\mu (\alpha_j^\dagger \alpha_{j+\hat{\mu}} + h.c.) \\ & + \Delta \sum_j (\alpha_j^\dagger \alpha_{j+\hat{1}}^\dagger - i \alpha_j^\dagger \alpha_{j+\hat{2}}^\dagger + h.c.) \\ & - \mu \sum_j (\alpha_j^\dagger \alpha_j - \alpha_j \alpha_j^\dagger), \end{aligned} \quad (\text{A4})$$

where $\tilde{t}_\mu = -b_\mu$, $\Delta = t$, and $\mu = m/2 - (b_x + b_y)$. H_b is likewise, and hence, it turns out that the Wilson-Dirac Hamiltonian (2) also describes (two copies of) a spinless $p + ip$ superconductor on a square lattice, or spinful one if H_a and H_b are regarded as the Hamiltonians for spin-up and -down parts. When $b_x = b_y \equiv b$, the chemical potential $\mu = 0$ at $m = 4b$, which is just the topological transition discussed by Read and Green.⁴⁶

- ¹ X.-L. Qi and S.-C. Zhang, Rev. Mod. Phys. **83**, 1057 (2011), URL <http://link.aps.org/doi/10.1103/RevModPhys.83.1057>.
- ² M. Z. Hasan and C. L. Kane, Rev. Mod. Phys. **82**, 3045 (2010).
- ³ J. E. Moore, Nature **464**, 194 (2010).
- ⁴ Y. Ando, Journal of the Physical Society of Japan **82**, 102001 (2013), <http://journals.jps.jp/doi/pdf/10.7566/JPSJ.82.102001>, URL <http://journals.jps.jp/doi/abs/10.7566/JPSJ.82.102001>.
- ⁵ P. Gehring, H. M. Benia, Y. Weng, R. Dinnebier, C. R. Ast, M. Burghard, and K. Kern, Nano Letters **13**, 1179 (2013), <http://pubs.acs.org/doi/pdf/10.1021/nl304583m>, URL <http://pubs.acs.org/doi/abs/10.1021/nl304583m>.
- ⁶ Y. Yoshimura, A. Matsumoto, Y. Takane, and K.-I. Imura, Phys. Rev. B **88**, 045408 (2013), URL <http://link.aps.org/doi/10.1103/PhysRevB.88.045408>.
- ⁷ K. Kobayashi, T. Ohtsuki, and K.-I. Imura, Phys. Rev. Lett. **110**, 236803 (2013), URL <http://link.aps.org/doi/10.1103/PhysRevLett.110.236803>.
- ⁸ C.-X. Liu, X.-L. Qi, and S.-C. Zhang, Physica E Low-Dimensional Systems and Nanostructures **44**, 906 (2012), 1110.3420.
- ⁹ J. Seo, P. Roushan, H. Beidenkopf, Y. S. Hor, R. J. Cava, and A. Yazdani, Nature **466**, 343 (2010).
- ¹⁰ Y. Takane, Journal of the Physical Society of Japan **73**, 2366 (2004), URL <http://jpsj.ipap.jp/link?JPSJ/73/2366/>.
- ¹¹ B. Rasche, A. Isaeva, M. Ruck, S. Borisenko, V. Zabolotnyy, B. B²uchner, K. Koepernik, C. Ortix, M. Richter, and J. van den Brink, Nature materials **12**, 422 (2013).
- ¹² L. Fu, Phys. Rev. Lett. **106**, 106802 (2011), URL <http://link.aps.org/doi/10.1103/PhysRevLett.106.106802>.
- ¹³ T. H. Hsieh, H. Lin, J. Liu, W. Duan, A. Bansil, and L. Fu, Nature Communications **3**, 982 (2012), URL <http://www.nature.com/ncomms/journal/v3/n7/full/ncomms1969.html>.
- ¹⁴ T. Morimoto and A. Furusaki, Phys. Rev. B **88**, 125129 (2013), URL <http://link.aps.org/doi/10.1103/PhysRevB.88.125129>.
- ¹⁵ Y. Tanaka, Z. Ren, T. Sato, K. Nakayama, S. Souma, T. Takahashi, K. Segawa, and Y. Ando, Nature Physics **8**, 800 (2012), URL <http://www.nature.com/nphys/journal/v8/n11/abs/nphys2442.html>.
- ¹⁶ P. Dziawa, B. Kowalski, K. Dybko, R. Buczko, A. Szczerbakow, M. Szot, E. Lusakowska, T. Balasubramanian, B. M. Wojek, M. Berntsen, et al., Nature Materials **11**, 1023 (2012).
- ¹⁷ A. A. Burkov and L. Balents, Phys. Rev. Lett. **107**, 127205 (2011), URL <http://link.aps.org/doi/10.1103/PhysRevLett.107.127205>.
- ¹⁸ B. Yan, L. Muehler, and C. Felser, Phys. Rev. Lett. **109**, 116406 (2012), URL <http://link.aps.org/doi/10.1103/PhysRevLett.109.116406>.
- ¹⁹ T. Fukui, K.-I. Imura, and Y. Hatsugai, Journal of the Physical Society of Japan **82**, 073708 (2013), <http://journals.jps.jp/doi/pdf/10.7566/JPSJ.82.073708>, URL <http://journals.jps.jp/doi/abs/10.7566/JPSJ.82.073708>.
- ²⁰ G. Yang, J. Liu, L. Fu, W. Duan, and C. Liu, Phys. Rev. B **89**, 085312 (2014), URL <http://link.aps.org/doi/10.1103/PhysRevB.89.085312>.
- ²¹ S. Ryu and Y. Hatsugai, Phys. Rev. Lett. **89**, 077002 (2002).
- ²² Y. Hatsugai, Solid State Communications **149**, 1061 (2009), ISSN 0038-1098, recent Progress in Graphene Studies, URL <http://www.sciencedirect.com/science/article/pii/S0038109809000000>.
- ²³ B. A. Bernevig, T. L. Hughes, and S.-C. Zhang, Science **314**, 1757 (2006), <http://www.sciencemag.org/content/314/5806/1757.full.pdf>, URL <http://www.sciencemag.org/content/314/5806/1757.abstract>.
- ²⁴ C.-X. Liu, X.-L. Qi, X. Dai, Z. Fang, and S.-C. Zhang, Nature Physics **5**, 438 (2010).
- ²⁵ C.-X. Liu, X.-L. Qi, H. Zhang, X. Dai, Z. Fang, and S.-C. Zhang, Phys. Rev. B **82**, 045122 (2010), URL <http://link.aps.org/doi/10.1103/PhysRevB.82.045122>.
- ²⁶ A. Yamakage, K. Nomura, K.-I. Imura, and Y. Kuramoto, Journal of the Physical Society of Japan **80**, 053703 (2011), URL <http://jpsj.ipap.jp/link?JPSJ/80/053703/>.
- ²⁷ A. Yamakage, K. Nomura, K.-I. Imura, and Y. Kuramoto, Phys. Rev. B **87**, 205141 (2013), URL <http://link.aps.org/doi/10.1103/PhysRevB.87.205141>.
- ²⁸ R.-J. Slager, A. Mesaros, V. Juričić, and J. Zaanen, Nature Physics **9**, 98 (2012), URL <http://www.nature.com/nphys/journal/v9/n2/full/nphys2513.html>.
- ²⁹ L. Fu and C. L. Kane, Phys. Rev. B **76**, 045302 (2007), URL <http://link.aps.org/doi/10.1103/PhysRevB.76.045302>.
- ³⁰ G. W. Semenoff, Phys. Rev. Lett. **53**, 2449 (1984), URL <http://link.aps.org/doi/10.1103/PhysRevLett.53.2449>.
- ³¹ Y. Hatsugai, M. Kohmoto, and Y.-S. Wu, Phys. Rev. B **54**, 4898 (1996), URL <http://link.aps.org/doi/10.1103/PhysRevB.54.4898>.
- ³² H. Watanabe, Y. Hatsugai, and H. Aoki, Phys. Rev. B **82**, 241403 (2010), URL <http://link.aps.org/doi/10.1103/PhysRevB.82.241403>.
- ³³ L. Fu, C. L. Kane, and E. J. Mele, Phys. Rev. Lett. **98**, 106803 (2007), URL <http://link.aps.org/doi/10.1103/PhysRevLett.98.106803>.
- ³⁴ J. E. Moore and L. Balents, Phys. Rev. B **75**, 121306 (2007), URL <http://link.aps.org/doi/10.1103/PhysRevB.75.121306>.
- ³⁵ R. Roy, Phys. Rev. B **79**, 195322 (2009), URL <http://link.aps.org/doi/10.1103/PhysRevB.79.195322>.
- ³⁶ K. Nakayama, K. Eto, Y. Tanaka, T. Sato, S. Souma, T. Takahashi, K. Segawa, and Y. Ando, Phys. Rev. Lett. **109**, 236804 (2012), URL <http://link.aps.org/doi/10.1103/PhysRevLett.109.236804>.
- ³⁷ Y. Hatsugai and S. Ryu, Phys. Rev. B **65**, 212510 (2002), URL <http://link.aps.org/doi/10.1103/PhysRevB.65.212510>.
- ³⁸ Y. Hatsugai, S. Ryu, and M. Kohmoto, Phys. Rev. B **70**, 054502 (2004), URL <http://link.aps.org/doi/10.1103/PhysRevB.70.054502>.
- ³⁹ T. Fukui, Y. Hatsugai, and H. Suzuki, Journal of the Physical Society of Japan **74**, 1674 (2005), URL <http://jpsj.ipap.jp/link?JPSJ/74/1674/>.
- ⁴⁰ M. Okamoto, Y. Takane, and K.-I. Imura, Phys. Rev. B **89**, 125425 (2014), URL <http://link.aps.org/doi/10.1103/PhysRevB.89.125425>.
- ⁴¹ X. Li, F. Zhang, Q. Niu, and J. Feng, ArXiv e-prints (2013), 1310.6598.
- ⁴² Y. Hatsugai, Phys. Rev. Lett. **71**, 3697 (1993), URL

- <http://link.aps.org/doi/10.1103/PhysRevLett.71.3697>.
- ⁴³ H. Obuse, S. Ryu, A. Furusaki, and C. Mudry, Phys. Rev. B **89**, 155315 (2014), URL <http://link.aps.org/doi/10.1103/PhysRevB.89.155315>.
- ⁴⁴ F. F. Assaad, T. C. Lang, and F. Parisen Toldin, Phys. Rev. B **89**, 125121 (2014), URL <http://link.aps.org/doi/10.1103/PhysRevB.89.125121>.
- ⁴⁵ K. Ejima and T. Fukui, Journal of the Physical Society of Japan **80**, 123708 (2011), <http://journals.jps.jp/doi/pdf/10.1143/JPSJ.80.123708>, URL <http://journals.jps.jp/doi/abs/10.1143/JPSJ.80.123708>.
- ⁴⁶ N. Read and D. Green, Phys. Rev. B **61**, 10267 (2000), URL <http://link.aps.org/doi/10.1103/PhysRevB.61.10267>.